

AARHUS UNIVERSITY

DEPARTMENT OF MECHANICAL AND PRODUCTION
ENGINEERING

DYNAMIC SYSTEMS WITH APPLICATION - GROUP 9

Wind Turbine Project

Student:

Frederik Fristed
Katharina Brarup Schäfer
Petar Gavran
Rune Marsilius Jensen
Thea Gorzelak

Student number:

201805718
201710730
202102200
201808110
201807917



AARHUS UNIVERSITY

May 23 2022

Symbols

RFT 3D

γ	=	Acceleration constraint equation
λ	=	Lagrange multipliers
Φ	=	Constraint equations
$\Phi_{\mathbf{P}}$	=	Jacobian of Euler parameter constraint function
$\Phi_{\mathbf{P}}^{\mathbf{P}}$	=	Euler parameter normalization jacobian
$\Phi_{\mathbf{r}}$	=	Jacobian of generalised coordinate constraint function
\mathbf{A}	=	Rotation matrix in terms of Euler parameters
$\mathbf{F}^{\mathbf{A}}$	=	Applied force
\mathbf{G}	=	G-matrix
\mathbf{J}'	=	Mass moment of inertia
\mathbf{M}	=	Mass matrix
nb	=	Number of bodies
$\mathbf{n}'^{\mathbf{A}}$	=	Applied torque
\mathbf{p}	=	Euler parameters
\mathbf{q}	=	Composite set of generalised coordinates
\mathbf{r}	=	Generalised cartesian coordinates
\mathbf{s}'^P	=	Position vector in the local reference frame
k_{θ}	=	Spring koefficient
c_{θ}	=	damping coefficient
θ	=	Relative angle of rotation
Ω	=	Rotational speed
U^{el}	=	Elastic potential energy
e	=	Eccentricity
E	=	Elastic modulus
I	=	Moment of inertia
y	=	Deflection
P	=	Point load
k	=	Stiffness
ζ	=	Damping ratio
c	=	Damping coefficient

RFT-B 2D

ν	=	Lateral deflection (time-dependent)
ω	=	Natural frequency
Ω	=	Rotational speed
ψ	=	Angular rotation (time-dependent)
ρ	=	Density
σ	=	Bending stress
A	=	Cross-sectional area
\mathbf{C}	=	Damping matrix
\mathbf{D}	=	Centrifugal damping matrix
e	=	Eccentricity
E	=	Elastic modulus
\mathbf{E}	=	Centrifugal stiffness matrix
g	=	Gravity
h	=	Height
\mathbf{H}	=	Frequency response function
I	=	Area moment of inertia
\mathbf{K}	=	Stiffness matrix
\mathbf{K}_G	=	Geometric stiffness matrix
L	=	Length
m	=	Mass
\mathbf{M}	=	Mass matrix
N	=	Lifetime in number of cycles
\mathbf{N}	=	Shape function
\mathbf{q}	=	Generalised coordinates
\mathbf{Q}_{el}	=	Elastic generalised forces
\mathbf{Q}_g	=	Gravitational generalised forces
\mathbf{Q}_v	=	Quadratic velocity forces
\mathbf{r}	=	Position vector in the global reference frame
T	=	Kinetic energy
\bar{u}_f	=	Spatial and time-dependent deflection
U	=	Potential energy
U_{el}	=	Elastic potential energy
U_g	=	Gravitational potential energy
V	=	Shear force
X	=	Response amplitude

Contents

1	Rotor with Flexible Tower 3D	1
1.1	Modelling of RFT in 3D as multibody system	1
1.2	Experiments and data acquisition	5
1.3	Comparison of results	6
1.4	Balancing of RFT system	10
1.5	Future improvement of RFT model	11
1.6	Conclusion	11
2	RFT-B 2D	12
2.1	Modelling of RFT-B	13
2.2	Campbell Diagram	14
2.3	Lateral Dynamic Response of Tower $\Omega = 120$ rpm	15
2.4	Lateral Dynamic Response of Tower $\Omega = 20 - 450$ rpm	17
2.5	Fatigue damage of the blades	19
2.6	Conclusion	20

1 | Rotor with Flexible Tower 3D

The first part of the project is concerned with a 3-dimensional model of the Rotor with Flexible Tower, which in the following will be denoted as the RFT system. The system is shown in Fig. 1.1, where the nacelle and rotor with an unbalance are modelled as rigid bodies and the tower is flexible and modelled with a number of lumped masses and rotational spring-damper joints.

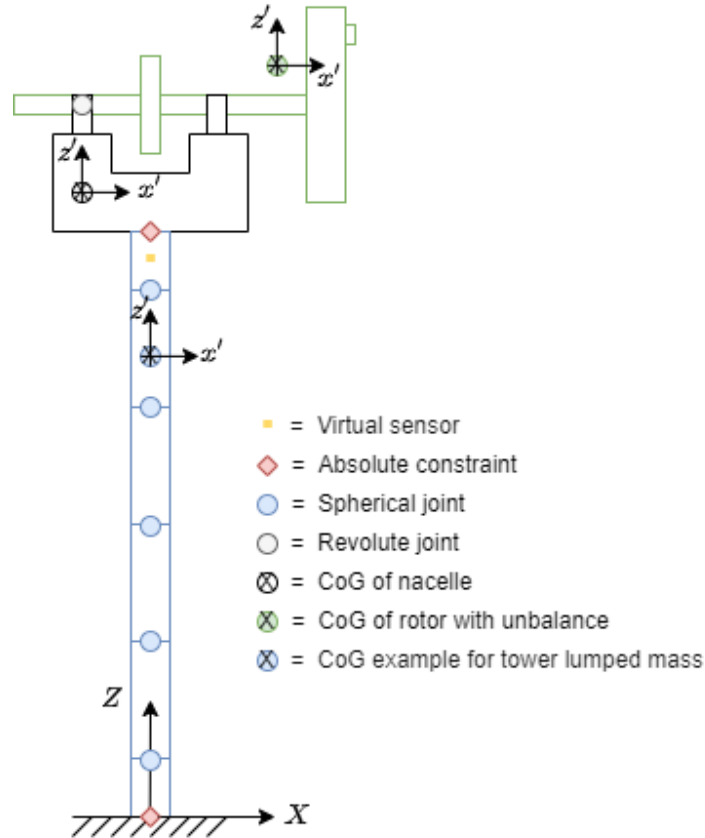


Figure 1.1: System drawing of the RFT in 3D

1.1 Modelling of RFT in 3D as multibody system

The RFT is modelled as a constrained spatial multibody system. Each body is described using three generalized coordinates, that describe the position of the center of gravity, and four Euler parameters that specify the orientation of the body. The composite set of generalized coordinates are denoted \mathbf{q} , see Eq. (1.1).

$$\mathbf{r} = [\mathbf{r}_1^T \quad \mathbf{r}_2^T \quad \dots \quad \mathbf{r}_{nb}^T]^T \quad \mathbf{p} = [\mathbf{p}_1^T \quad \mathbf{p}_2^T \quad \dots \quad \mathbf{p}_{nb}^T]^T \quad \mathbf{q} = [\mathbf{r}_1^T \quad \mathbf{p}_1^T \quad \dots \quad \mathbf{r}_{nb}^T \quad \mathbf{p}_{nb}^T]^T \quad (1.1)$$

Due to the orientation of the local coordinate system, see Fig. 1.1, the initial rotation of all bodies is zero. The initial generalized coordinates are determined using the initial rotation around the y-axis and the local vectors from between the centers of gravity and the joints. The

initial Euler parameters are determined using the initial orientation of the local coordinate systems. The tower is modelled flexibly using the lumped mass method. The first and last lumped masses are shorter than the middle ones, because they are absolutely constrained to the ground and nacelle respectively. The lumped masses of the tower are connected to each other using spherical joints, and the rotor is connected to the nacelle using a revolute joint, see Fig. 1.1. The individual lumped masses are modelled rigidly. The constraints for each joint is set up using basic constraints. The constraints for the spherical joints are given by Eq. (1.2).

$$\Phi^s(P_i, P_j) = \mathbf{r}_j + \mathbf{A}_j \mathbf{s}_j^P - \mathbf{r}_i - \mathbf{A}_i \mathbf{s}_i^P = \mathbf{0} \quad (1.2)$$

The Φ^s constraint imposes that a point, P_i , on body i always coincides with a point, P_j , on body j . There are no constraints regarding rotation between the two bodies.

The revolute joint between the rotor and the nacelle is modelled by adding a parallel-1 constraint, see Eq. (1.3), to the spherical joint. This constraint imposes that the local coordinate systems each have two axis that are parallel in pairs. This means that rotation between the two bodies is locked around two out of three axes.

$$\begin{aligned} \Phi^s(P_i, P_j) &= \mathbf{0} \\ \Phi^{p1}(\mathbf{h}_i, \mathbf{h}_j) &= \mathbf{0} \end{aligned} \quad (1.3)$$

The parallel-1 constraint consists of two dot-1 constraints, see Eq. (1.4).

$$\Phi^{p1}(\mathbf{h}_i, \mathbf{h}_j) = \begin{bmatrix} \Phi^{d1}(\mathbf{f}_i, \mathbf{h}_j) \\ \Phi^{d1}(\mathbf{g}_i, \mathbf{h}_j) \end{bmatrix} = 0 \quad (1.4)$$

The dot-1 constraint imposes that two vectors fixed in their respective bodies are orthogonal, i.e. that their scalar product is zero.

$$\Phi^{d1}(\mathbf{a}_i, \mathbf{a}_j) = \mathbf{a}_i^T \mathbf{a}_j = \mathbf{a}_i'^T \mathbf{A}_i^T \mathbf{A}_j \mathbf{a}_j' = 0 \quad (1.5)$$

The first and last lumped masses of the tower are absolutely constrained to the ground and nacelle respectively, meaning that all degrees of freedom between the ground and body or between the two bodies are locked. The model is calculated using the Euler parameter system acceleration equation, see Eq. (1.6).

$$\begin{bmatrix} \mathbf{M} & \mathbf{0} & \Phi_r^T & \mathbf{0} \\ \mathbf{0} & 4\mathbf{G}^T \mathbf{J} \mathbf{G} & \Phi_p^T & \Phi_p^{PT} \\ \Phi_r & \Phi_p & \mathbf{0} & \mathbf{0} \\ \mathbf{0} & \Phi_p^P & \mathbf{0} & \mathbf{0} \end{bmatrix} \cdot \begin{bmatrix} \ddot{\mathbf{r}} \\ \ddot{\mathbf{P}} \\ \lambda \\ \lambda^P \end{bmatrix} = \begin{bmatrix} \mathbf{F}^A \\ 2\mathbf{G}^T \mathbf{n}'^A + 8\dot{\mathbf{G}}^T \mathbf{J} \dot{\mathbf{G}} \mathbf{p} \\ \gamma \\ \gamma^P \end{bmatrix} \quad (1.6)$$

The applied forces consist of the gravity acting on each body. The internal forces in the joints are modelled using a rotational spring-damper actuator (RSDA). The torque exerted by the RSDA is calculated as shown in Eq. (1.7).

$$n'^A = k_\theta(\theta + 2n_{rev}\pi) + c_\theta\dot{\theta} + N(\theta + 2n_{rev}\pi, \dot{\theta}) \quad (1.7)$$

$N(\theta + 2n_{rev}\pi, \dot{\theta})$ is the general actuator torque. This term is zero in the model, because no actuator is present. A relative rotational driver is added to the rotor to make it spin around the rotational axis of its revolute joint.

$$\Phi^{rot} = \theta + 2n\pi - C(t) = 0 \quad C(t) = 2\pi \cdot \frac{\Omega}{60} \cdot t \quad (1.8)$$

The rotor rotates at constant velocity and therefore needs an initial velocity. The initial velocity is given by the angular velocity multiplied with the in-plane offset.

Identification of parameters

Table 1.1 shows parameters of the RFT system measured during the experiment.

Description	Symbol	Value
Height of tower	h^{tower}	1.69 m
Unbalanced mass	m^{un}	0.082 kg
Eccentricity of unbalanced mass	l^{ecc}	0.096 m
Tower width	w	0.03 m
Tower depth	d	0.02 m
Tower wall thickness	δ^{tw}	0.002 m
Radius of rotor	r^{rot}	0.0125 m
Distance from bottom of nacelle to sensor	d^{sen}	0.020 m

Table 1.1: System parameters and conditions of the experiment

Stiffness of joints

Several different approaches can be taken when calculating the bending stiffness of the spherical joints. In this report, Rayleigh's Energy method is considered. The system considered is a clamped beam in static equilibrium after being subjected to an arbitrary point load P in the free end. Eq. (1.9) shows the elastic energy of a continuous beam, U_{cont}^{el} , where $y(x)$ is the deflection.

$$U_{cont}^{el} = \int_0^{h_{red}^{tower}} E \cdot I_x \cdot y(x)'' dx \quad y(x) = -\frac{P \cdot x^2}{6 \cdot E \cdot I} \cdot (3 \cdot h_{red}^{tower} - x) \quad (1.9)$$

h_{red}^{tower} is the height of the tower without the first and last lumped masses of the tower. The equivalent elastic energy of a discrete beam with nb bodies is shown in Eq. (1.10).

$$U_{disc}^{el} = \frac{1}{2} \cdot k_t \cdot \sum_{i=1}^{nb} \left(y' \left(\frac{h_{red}^{tower}}{nb} \cdot i \right) - y' \left(\frac{h_{red}^{tower}}{nb} \cdot (i-1) \right) \right)^2 \quad (1.10)$$

Setting Eq. (1.9) equal to Eq. (1.10) and isolating k_t yields Eq. (1.11).

$$k_t = \frac{41 \cdot nb^3 \cdot E \cdot I}{h_{red}^{tower} \cdot (4 \cdot nb^2 - 1)} \quad (1.11)$$

This expression assumes that the bending stiffness is the same in a direction for all spherical joints. Because the tower has a rectangular cross section, the stiffness in the fore-aft direction, k_t^{fa} , is higher than the stiffness in the transverse direction, k_t^{tv} , because I_y is higher than I_x .

For $nb=11$ this results in a stiffness of 15.3 kNm/rad in the transverse direction and 29.5 kNm/rad in the fore-aft direction. The torsional stiffness about the Z-axis is calculated using the shear modulus of steel, G , and the tower's polar moment of inertia, J' . In the next section, the damping coefficient is calculated from experimental data using the logarithmic decrement method. This is shown in Section 1.2.

Virtual sensor

For the verification of the RFT model, it has to be compared to experimental data and other models, and in order to get the motion of the system at the same reference point, a virtual sensor is installed. The virtual sensor is installed $d^{sen} = 0.02$ m below the nacelle in the Z-direction

and aligned with origo of the global reference frame for the X- and Y-direction. The motion of the virtual sensor is tracked using Eq. (1.12), where \mathbf{r} is the CoG of the last body of the tower.

$$\mathbf{r}^P = \mathbf{r} + \mathbf{A}\mathbf{s}'^P \quad \dot{\mathbf{r}}^P = \dot{\mathbf{r}} + \mathbf{A}\tilde{\omega}'\mathbf{s}'^P \quad \ddot{\mathbf{r}}^P = \ddot{\mathbf{r}} + (\mathbf{A}\tilde{\omega}' + \mathbf{A}\tilde{\omega}'\tilde{\omega}')\mathbf{s}'^P \quad (1.12)$$

Convergence study

A convergence study is performed to determine the minimum number of bodies nb_{min} required to obtain reliable results. The 3D simulation is run for rotational speeds $\Omega = 210$ rpm and $\Omega = 400$ rpm for number of bodies in the range $nb = 5-12$. Fig. 1.2 shows the maximum deflection of the virtual sensor in the fore-aft direction vs. the maximum deflection in the transverse direction. The criteria for convergence is defined as $\leq 5\%$ change in both directions compared to the previous number of bodies. This leads to a total number of bodies of $nb = 11$ for converged results.

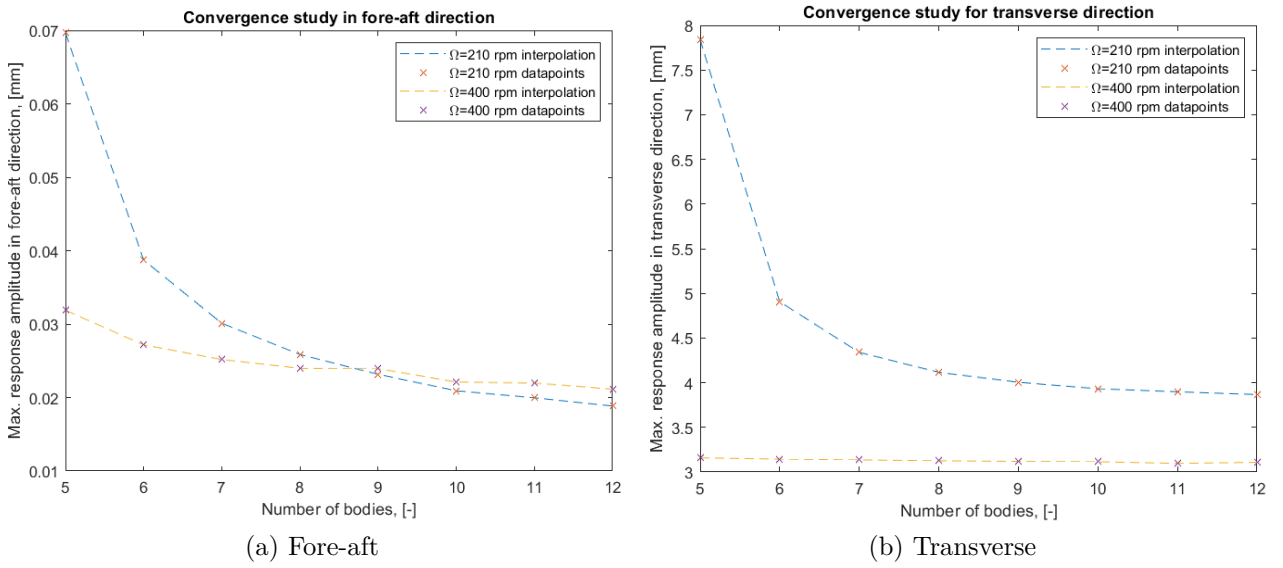


Figure 1.2: Frequency Response Function for acceleration

Alternative models - 2DoF and 5DoF

In earlier lectures, two continuous models have been developed for the wind turbine with unbalanced rotor. The 2DoF model has one translational DoF in both the transverse and fore-aft direction. The 5DoF model has one translational and one rotational DoF in both the transverse and fore-aft direction and also has a DoF for the axial rotation of the tower. This report will not go into detail regarding how the models are defined. In later sections, results from the 3D multibody RFT are compared to the 2DoF and 5DoF models as well as the experimental results. To use the developed 2DoF and 5DoF models, the parameters are adjusted to fit the experiment. The vector from the top of the tower to the CoG of the nacelle, and the distance from the nacelle's CoG to the rotor are found from the CAD model. The distance from the center of the unbalanced rotor to its CoG is calculated in Eq. (1.13)

$$e = \frac{m_{unbalanced} \cdot l^{ecc}}{m_{rotor} + m_{unbalanced}} = 0.0035 \text{ m} \quad (1.13)$$

For the tower, the height and cross sectional properties are updated. The Youngs modulus E , shear modulus G and Poissons ratio ν are taken from 'Materials Science and Engineering'. The mass of the rotor and nacelle are found the CAD model.

1.2 Experiments and data acquisition

Experimental setup

An experiment is performed in the Dynamics Laboratory at Navitas. The experiment consists of a 1.69 meter long rectangular steel tube, which is welded and fastened to a steel plate. On top of the tube, a nacelle is constructed from 4 steel tubes and 2 bearings. A driveshaft is added to the bearings, with an electric motor in one end, and a weighted rotor in the other end. Between the bearings a counterweight is mounted. Approximately 1.67 meters from the ground, two high-end accelerometers and position sensors are mounted. Also, the accelerometer for the Arduino is mounted. The power supply is set to various constant voltages corresponding to various rotational speeds. Due to the unbalanced mass and the power of the motor, the measured rotational speeds have variations in the range of a few rpm for each voltage. In this project, the rotational speeds are assumed to be constant at the average value for each voltage.

Data acquisition

The acquisition of the data from the arduino accelerometer is done in a matlab script, which writes a 45sec .txt file with the measurements. Afterwards, the data is calibrated, and the amplitude and frequency is found and plotted to determine the values for the high- and low-pass filter. After the filtering the acceleration in the fore-aft and transverse direction is plotted. The acceleration and position from the other sensors are given in an excel file. To get the position in meters, the mean value of the extracted position is subtracted from all the data points, since the sensor measures the total position. These values are multiplied with 0.05 to convert the voltage output to meters. To get the acceleration in $[\frac{m}{s^2}]$ the voltage output is divided by 0.102 to convert to G and multiplied by 9.81 to convert to $[\frac{m}{s^2}]$. The mean value is then extracted because of a small offset. The data is filtered the same way as the arduino data.

The velocity is calculated both from the acceleration and from the position. From the acceleration, the velocity is calculated by numerical integration, and the drift is removed with the built in function "detrend" which removes the best straight fit line from the data. From the position, the velocity is calculated with the numerical differentiation method central finite differences. After numerical integration and differentiation it becomes clear that the accelerometer get the best results from the high frequency and the position sensor get the best results from the low frequency.

Damping coefficient

To acquire the damping coefficient, two free damped vibration experiments are performed, where acceleration and displacement are measured without any excitation from the motor. The signals are filtered the same way as before and the peaks of the outputs are found using the built-in Matlab function 'findpeaks'. Using these peaks, the damping ratio is calculated in Eq.(1.14) using the logarithmic decrement.

$$\zeta = \frac{1}{2\pi n} \log \frac{X_0}{X_n} \quad (1.14)$$

Based on the experiments, the RFT system has a damping ratio of $\zeta = 0.0013$ in the transverse direction and $\zeta = 0.0015$ in the fore-aft direction. To obtain the damping coefficient, c_t , the

tower is considered as a cantilever beam with a lumped mass in the free end.

$$m_{eq} = \frac{33}{140} \cdot m_{tower} + m_{nacelle} + m_{rotor} \quad k_{eq} = \frac{3 \cdot E \cdot I}{(h_{red}^{tower})^3} \quad c_c = 2 \cdot \sqrt{k_{eq} \cdot m_{eq}} \quad (1.15)$$

The damping coefficients are obtained using Eq. (1.16) and Eq. (1.15).

$$c = c_c \cdot \zeta \quad (1.16)$$

Using this approach, a damping coefficient of $c_{tv}=0.41$ Ns/m in the transverse direction and $c_{fa}=0.49$ Ns/m in the fore-aft direction is determined. These damping coefficients are assumed to be the same as the rotational damping in the spherical joints.

1.3 Comparison of results

The 3D multibody RFT model is simulated for $nb=11$ for 30s using a time step of 0.001s. A fine tolerance of 10^{-12} is used. In Eq. (1.11) and Eq. (1.16) the stiffness and damping coefficient for the spherical joints are calculated. However, this combination of stiffness and damping causes the model to become slow and unstable. To stabilize the model, a lower stiffness of $k_t=10$ kNm/rad and a lower damping coefficient of $c_t=0.01$ Nms/rad is assumed in both directions. In this report, results are shown for the rotational speed $\Omega=210$ rpm in Fig. 1.8. Results are shown in both time domain and frequency domain for both displacement and acceleration. Results for $\Omega=210$ rpm are also shown for experimental data in Fig. 1.4 and for the 2DoF/5DoF models in Fig. 1.7 and Fig. 1.6 respectively. Results are shown in time domain and frequency domain.

Frequency response functions

For rotational speeds in the range $\Omega=50-400$ rpm the frequency response function (FRF) is obtained for the 3D multibody RFT. This is compared to FRF from the experiment and the FRF from the continuous 2DoF and 5DoF models. For the RFT model, for each rotational speed a 5s simulation is performed and the maximum amplitude and corresponding frequency is determined. Due to computational limitations, the FRF is initially obtained with resolution in Ω of 10 rpm. To accurately determine the natural frequency, a finer resolution of 2 rpm is used in the area $\Omega=238-252$ rpm around the interesting area. For the continuous 5DoF and 2DoF models a constant resolution in Ω of 2 rpm is used. For the experiment, the resolution is determined by the number of experiments performed. For most of the experiments the resolution in Ω was 30 rpm. Fig. 1.3 shows the amplitude and frequency response for all models.

In Fig. 1.3, both the experiment and 2DoF/5DoF models show a significant peak around the rotational speed $\Omega = 120$ rpm in the transverse direction, corresponding to a transverse natural frequency of $\omega=2$ Hz. In the experimental data, the fore-aft direction appears to have a similar natural frequency to the transverse, but it is hard to tell because of the resolution of Ω in the experiment. In the 2DoF/5DoF, the fore-aft natural frequency is slightly higher around $\omega=2.5$ Hz in the 5DoF model and $\omega=3.33$ Hz in the 2DoF model. Compared to the experimental data, the 2DoF/5DoF model both overestimate the displacement/acceleration amplitude around the natural frequency by a factor of 2.

1.3. COMPARISON OF RESULTS

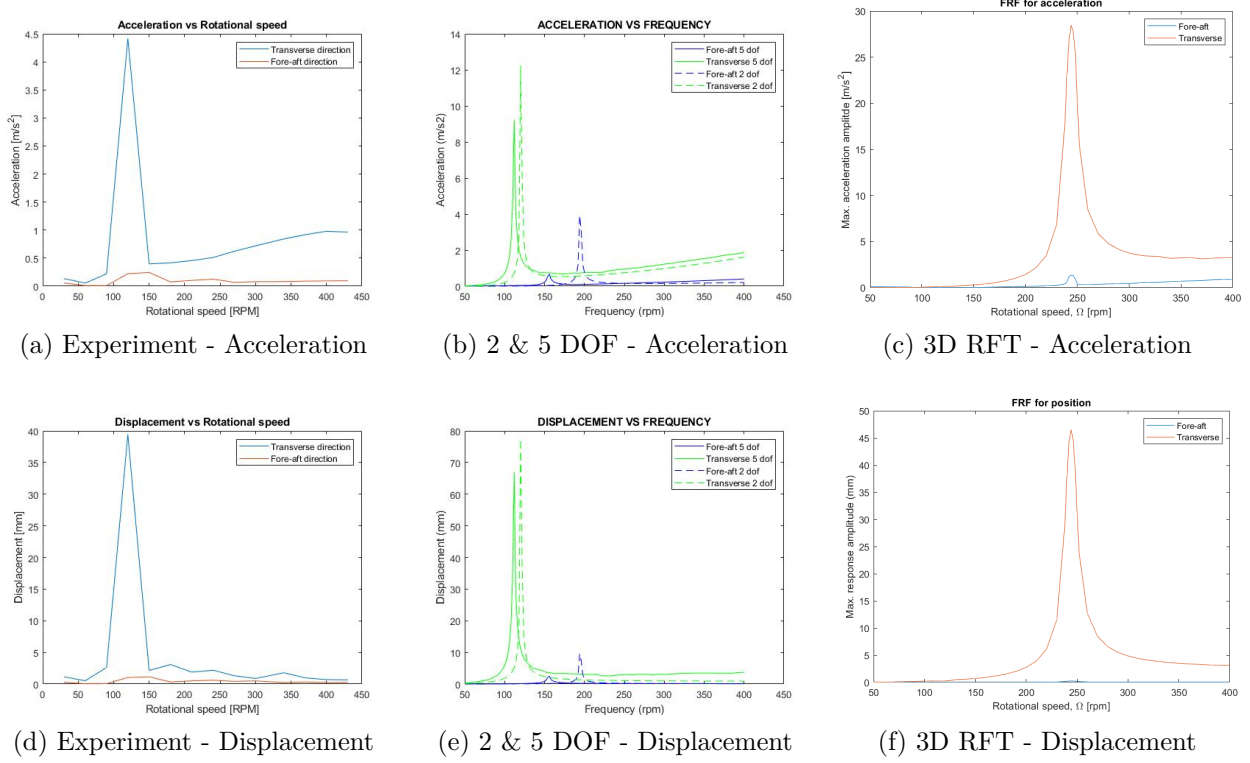


Figure 1.3: FRF for acceleration and position for the four different models

Fig. 1.3 (c) and (f) shows that the 3D multibody RFT model has a significantly higher natural frequency of 4.06 Hz (244 rpm) in both the transverse and fore-aft direction. This indicates that the stiffness used in the spherical joints of the 3D RFT model is not equivalent to the actual stiffness in the tower. In Eq. (1.11) a stiffness k_t of the spherical joint is calculated using Rayleigh's energy method. For $nb=11$ this results in a stiffness of 15.3 kNm/rad in the transverse direction and 29.5 kNm/rad in the fore-aft direction. These relatively high stiffnesses cause the 3D RFT model to become slow and unstable. Instead a lower stiffness of 10 kNm/rad is used in both directions. However, the high natural frequency of the 3D RFT model could indicate that this stiffness is still too high, as a reduction in stiffness would reduce the natural frequency. The general shape of the FRF from the 3D RFT model is very similar to the FRF from the experiment data. The 3D RFT model also matches the amplitude of the experiment closely in displacement. For better results, stiffness and damping in the spherical joints should be tweaked to tune in the natural frequency of the 3D RFT model to the values from the experiment.

Comparison in time and frequency domain

Comparing the experimental results in Fig. 1.4 with the 5 DoF model results in Fig. 1.5 and Fig. 1.6 shows overall good coherence. From the frequency domain figures, it can be read that the number of dynamic features represented by spikes are in agreement, as well as the frequencies they occur at. For the experimental data, the amplitude of both the position and acceleration is steady state from the beginning. The response for the 5 DoF model has a clear transient part that dies out at approximately 30 s, before it becomes steady state. The shape of the response functions in time domain for the experiment and 5 DoF model look similar with a beating effect, and the initial values for both position and acceleration are similar. The steady state position and acceleration of the 5DoF model is lower but still in the same range.

1.3. COMPARISON OF RESULTS

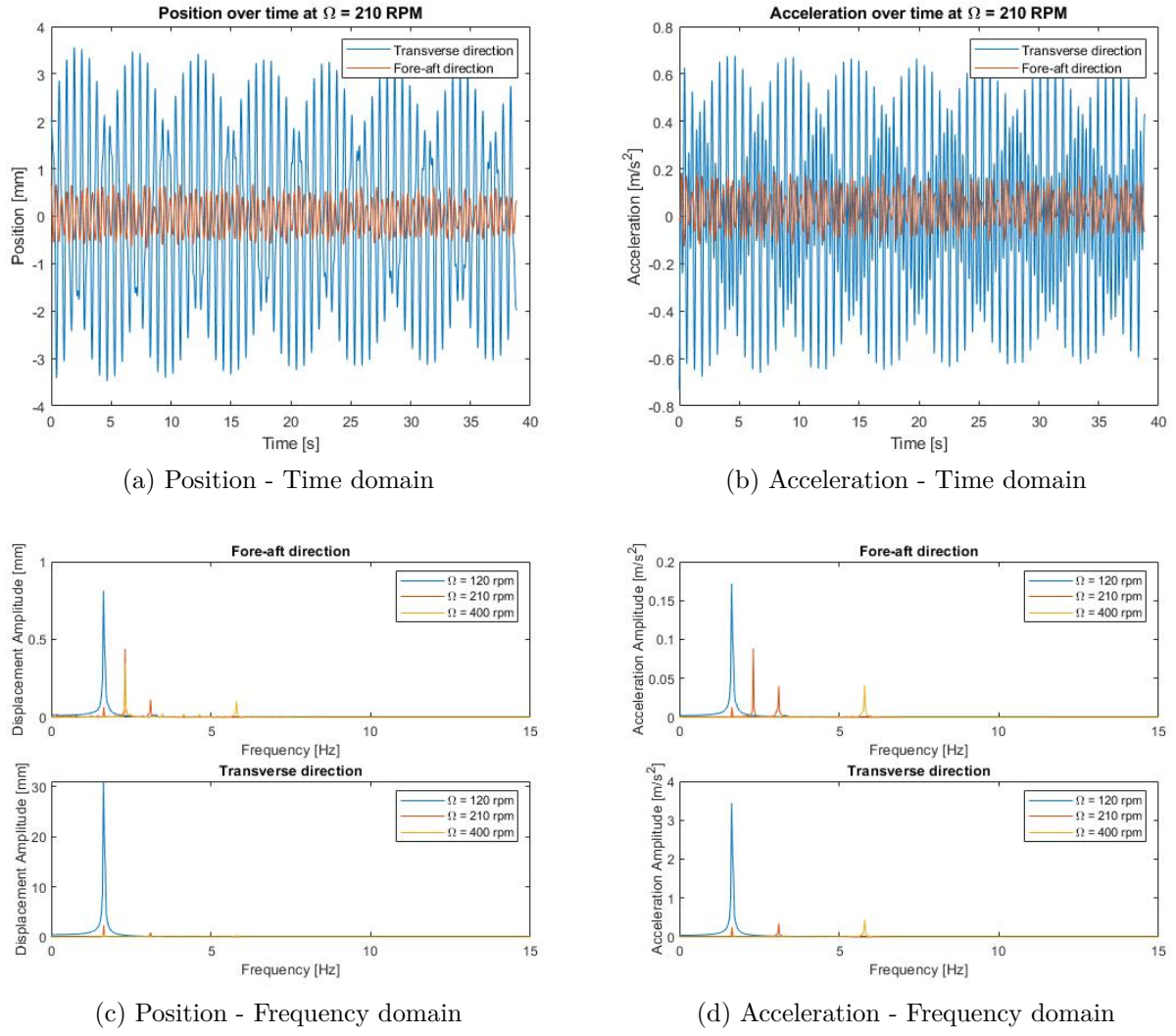


Figure 1.4: Results from the experiment in frequency and time domain.

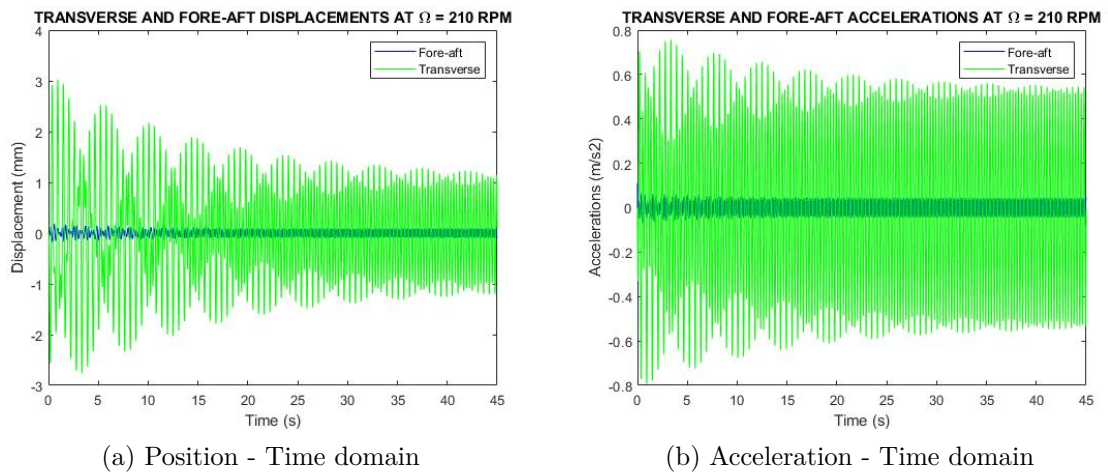


Figure 1.5: Results for the 5 DoF model in time domain

1.3. COMPARISON OF RESULTS

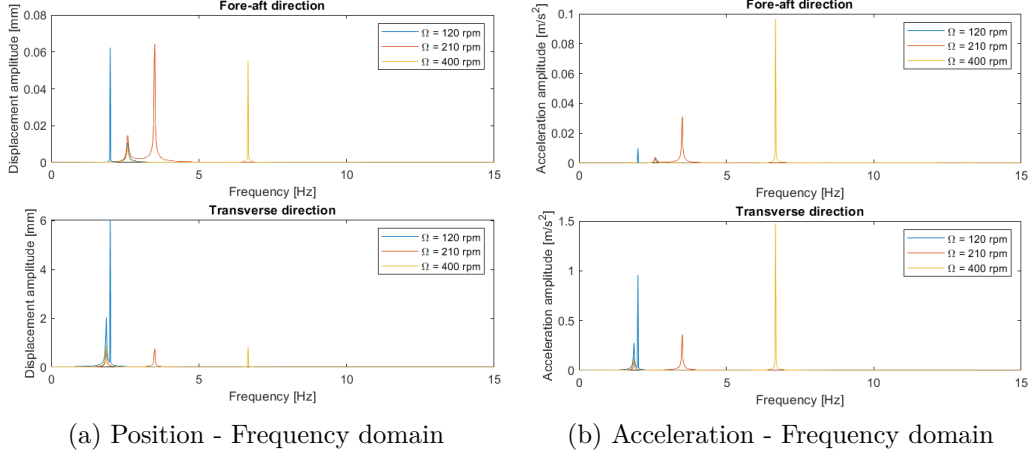


Figure 1.6: Results for the 5 DoF model in frequency domain

When comparing the experiment and 5 DoF model results to the 2 DoF model results shown in Fig. 1.7, it is clear that there are fewer dynamic features, which is a result of simplifying the whole system to one equivalent spring-mass element. However, the frequencies that are represented are in agreement with the main features of the experiment and 5 DoF model. Note that the response amplitude in the transverse direction is very high, which is due to resonance as shown on Fig. 1.3.

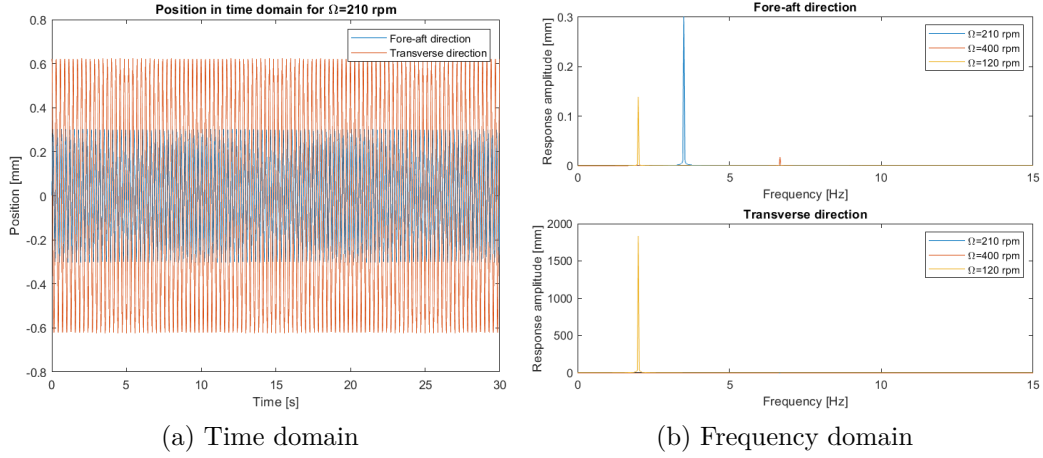


Figure 1.7: Results for 2 DoF model in time and frequency domain

Fig. 1.8 shows the obtained RFT model results. The transverse position amplitude from the time domain is equivalent to the amplitude of the experiment. The displacement amplitude in the fore-aft direction is small, compared to all the other models, which implies that the stiffness in the fore-aft direction is too high for the RFT model compared to the other models.

The shape of the displacement and acceleration signals have the beating effect as identified for the experiment and 5 DoF model, but the beating seems more frequent. When looking at the results in frequency domain, it can be read that the RFT model has the same number of dynamic features compared to the experiment and 5 DoF model, however, they occur at slight offset frequencies, for both the displacement and acceleration signals for $\Omega = 120$ rpm and $\Omega = 210$ rpm. Comparing the frequency domain results for a rotational speed of $\Omega = 400$ rpm shows better coherence between the RFT model and the experiments and 5 DoF model. This might be a result of the RFT model having a natural frequency close to $\Omega = 210$ rpm, and the

other models have a natural frequency close or equal to $\Omega = 120$ rpm, so the chosen rotational speeds for comparison might be impacted by the nearby natural frequencies.

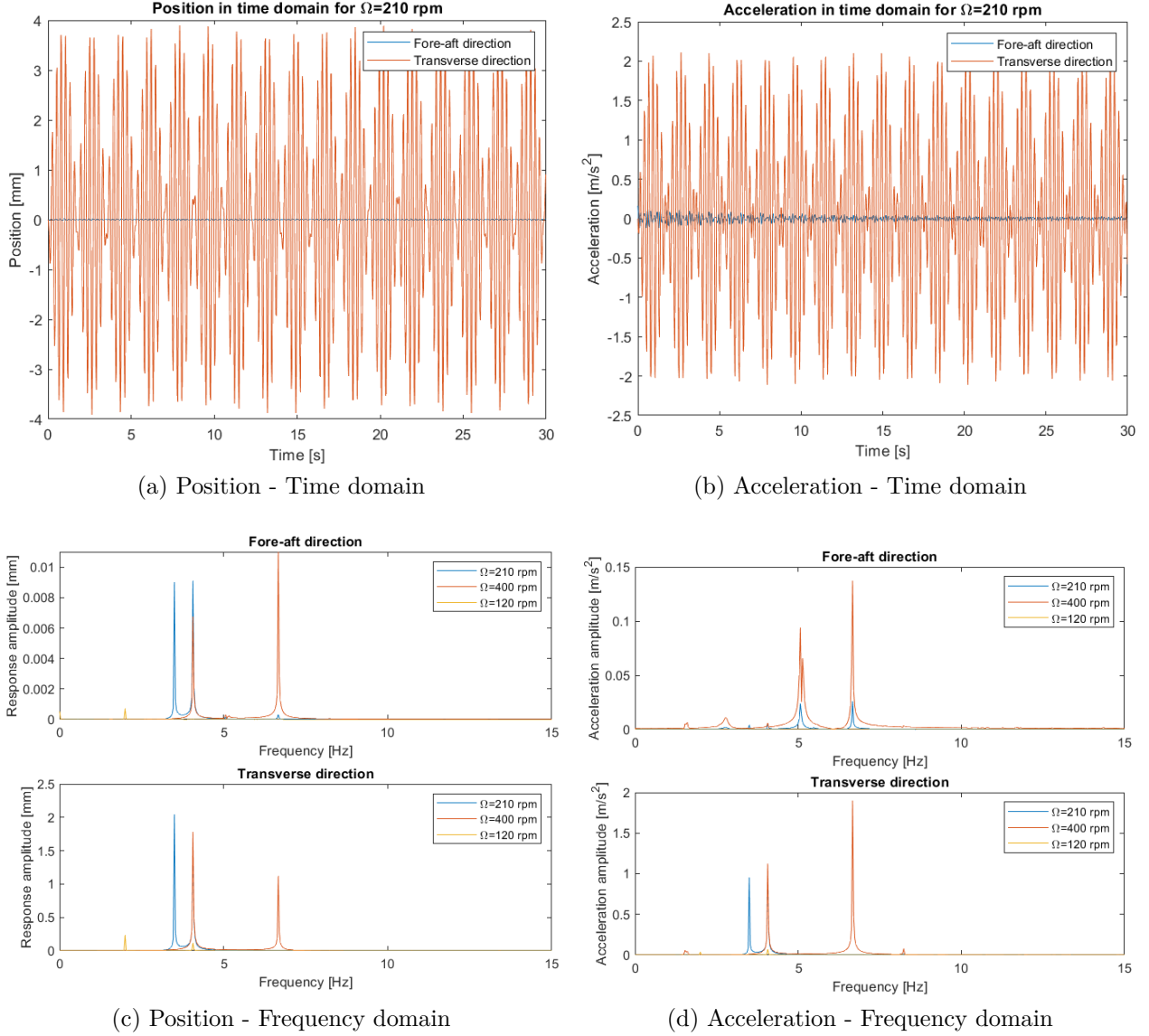


Figure 1.8: Results for the multibody RFT model in time and frequency domain.

1.4 Balancing of RFT system

The unbalance causes oscillation of the RFT system, which can be reduced by installing a virtual counterweight to balance the system. The counterweight has to be installed in the balancing plate behind the rotor, as shown on Fig. 1.1, which has a set eccentricity of 55 mm. To calculate the mass of the counterweight to balance the system statically, the condition in Eq. (1.17) is used.

$$\sum^2 m_i \cdot \Omega^2 \cdot \mathbf{r}_i = \mathbf{0} \quad (1.17)$$

The condition yields two equations, and can therefore be solved to two unknown: the mass $m_b = 143.13$ g and the orientation in relation to the unbalanced mass $\theta = 180^\circ$. Running the simulation of the RFT model with the counterweight yields the results shown in Fig. 1.9. It is clear, that the response amplitude is significantly lower in the transverse direction, meaning that the counterweight is in fact balancing the system.

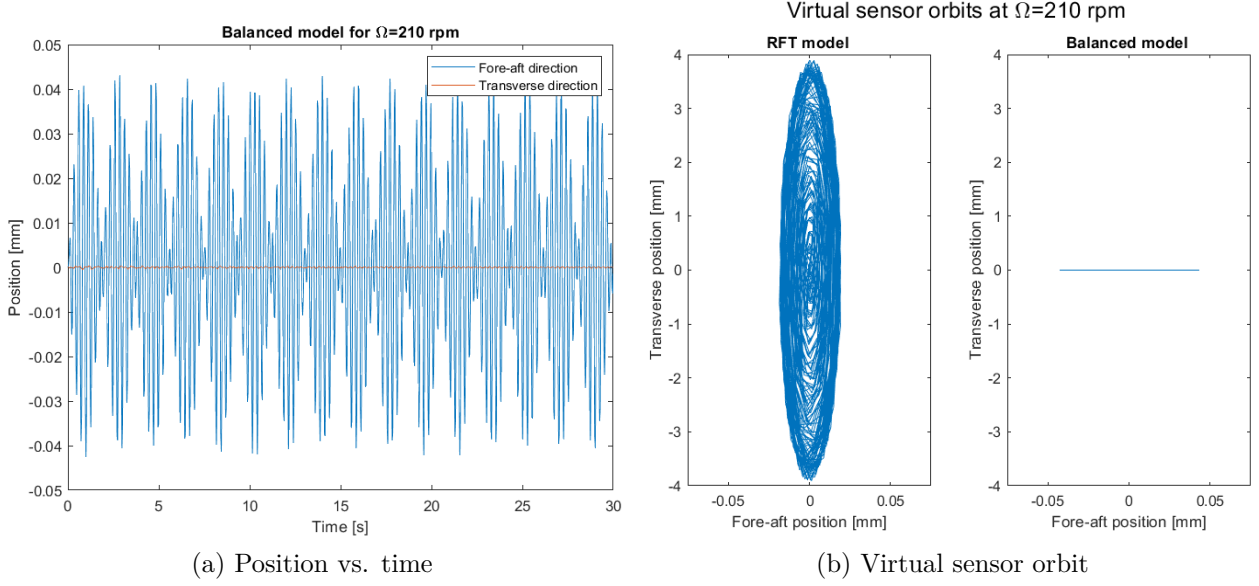


Figure 1.9: Results from the balanced RFT system

The counterweight is not balancing the system in the fore-aft direction, since the response amplitudes are higher, which can be read from the orbit. This is as expected, since it is not possible to balance the system in the fore-aft direction, because the balancing plate is at a fixed distance. However, the vibrations of the system have been significantly reduced.

1.5 Future improvement of RFT model

As discussed in the previous sections, the developed 3D multibody RFT model is somewhat inconsistent with the experimental results and the continuous 2DoF/5DoF models. The frequency response functions for the RFT models, shown in Fig. 1.3, are similar in shape to the ones obtained from the experiment, but the natural frequency of the RFT is off by a factor of 2, and amplitudes are inconsistent with the experiment. It is likely that the stiffness of the spherical joints plays a major role in these inconsistencies. In future improvements, the stiffness should be tweaked to tune in the multibody RFT to the experimental results. An alternative approach could be to use different stiffnesses in each joint to better approximate the shape functions used in the continuous models.

1.6 Conclusion

In the first part of the project, a 3-dimensional multibody model has successfully been developed for simulating the dynamics of a Rotor with Flexible Tower with an unbalance mass. The RFT model is compared to experimental data and 2DoF/5DoF models, but the results are not consistent; most importantly, the RFT model has a natural frequency of 4 Hz, which is a factor two bigger compared to the experiment and 2DoF/5DoF models. The inconsistencies of the model are most likely a result of the used stiffness and damping for the RSDA joints.

2 | RFT-B 2D

The second part of the project is concerned with a 2-dimensional model of the Rotor with Flexible Tower and Blades, which in the following will be denoted as the RFT-B system. The system is shown in Fig. 2.1 (a), and consists of 6 bodies, where the tower (body 1) and all three blades (bodies 4-6) are modelled as flexible bodies and the nacelle (body 2) and the hub (body 3) are modelled as rigid bodies. Blades 4 and 5 both have additional point masses, which will cause unbalance in the system. Blade 6 has no point mass.

To describe the system, a set of flexible generalised coordinates \mathbf{q} are used:

$$\mathbf{q} = [\nu^1 \quad \psi^1 \quad \nu^4 \quad \psi^4 \quad \nu^5 \quad \psi^5 \quad \nu^6 \quad \psi^6]^T \quad (2.1)$$

Since the nacelle and hub are modelled as rigid bodies, they are not represented by the flexible coordinates. Fig. 2.1 (b) shows how the flexible coordinates are defined for the tower and blade 4, where ν is the lateral deflection in the end point in the X-direction in the body frames and ψ is the angular rotation relative to the Y-axis in the body frames.

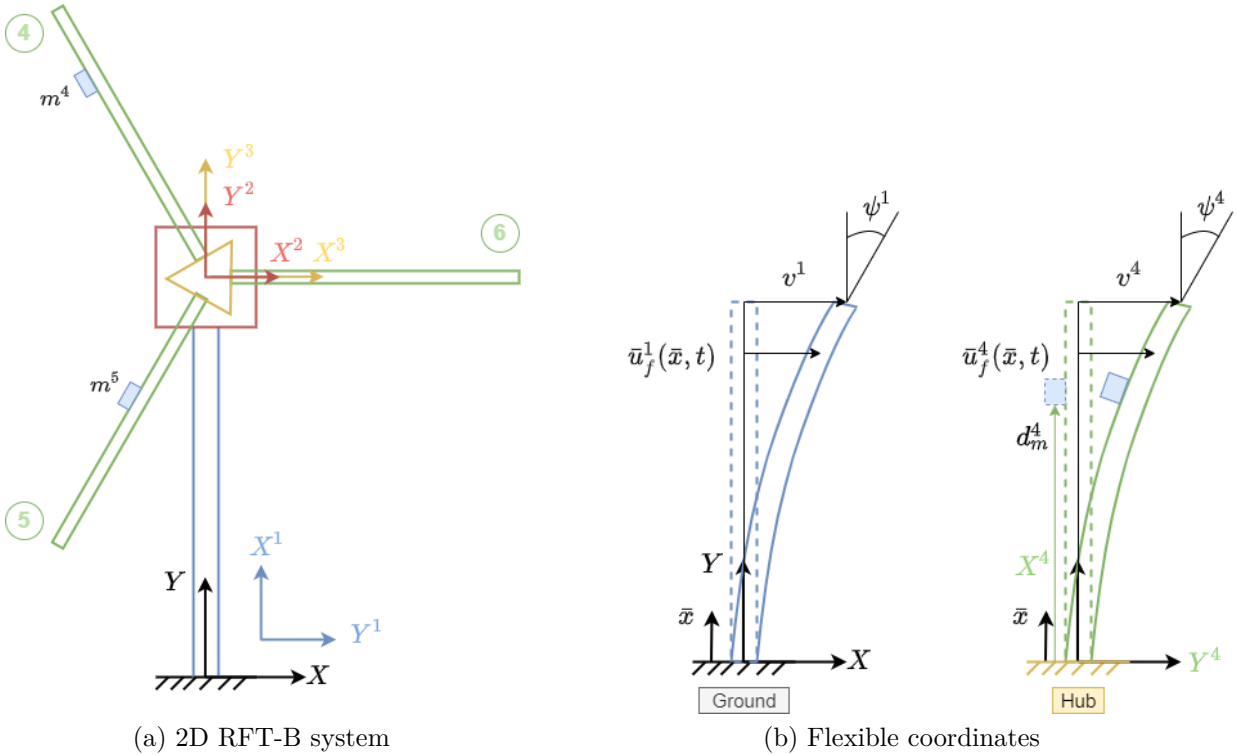


Figure 2.1: System drawing of 2D RFT-B and illustration showing flexible coordinates for tower (body 1) and blade with unbalance mass (body 4)

The following sections will go through how the RFT-B system is modelled as a multibody system using the Lagrange formulation, and perform a simulation of the system for firstly, a rotational speed of $\Omega = 120$ rpm, and secondly, for rotational speeds from $\Omega = 20 - 450$ rpm.

2.1 Modelling of RFT-B

Equations of motions (EOMs) are derived using a variation of Lagrange's equations.

$$\mathbf{M} = \frac{\partial}{\partial \dot{\mathbf{q}}} \left(\frac{\partial T}{\partial \dot{\mathbf{q}}} \right) \quad \mathbf{Q}_{el} = -\frac{\partial U}{\partial \mathbf{q}} \quad \mathbf{K} = -\frac{\partial \mathbf{Q}_{el}}{\partial \mathbf{q}} \quad \mathbf{Q}_g = -\frac{\partial U_g}{\partial \mathbf{q}} \quad (2.2)$$

$$\mathbf{Q}_v = -\frac{\partial}{\partial \mathbf{q}} \left(\frac{\partial T}{\partial \dot{\mathbf{q}}} \right) \cdot \dot{\mathbf{q}} - \frac{d}{dt} \left(\frac{\partial T}{\partial \dot{\mathbf{q}}} \right) + \frac{\partial T}{\partial \mathbf{q}} \quad \mathbf{E} = \frac{\partial \mathbf{Q}_v}{\partial \mathbf{q}} \quad \mathbf{D} = \frac{\partial \mathbf{Q}_v}{\partial \dot{\mathbf{q}}} \quad (2.3)$$

Where M is the mass matrix, K is the stiffness matrix, Q_{el} is the elastic generalized forces, Q_g is the gravitational generalized forces and Q_v is the quadratic velocity forces. E is the centrifugal stiffness matrix and D is the centrifugal damping matrix. The matrices are derived using the kinetic energy T and the potential energy U for all six bodies. Here, U is the sum of the elastic potential energy U_{el} and the gravitational potential energy U_g . In state space formulation, the equation of motion is:

$$\mathbf{M} \cdot \ddot{\mathbf{q}} + \mathbf{C} \cdot \dot{\mathbf{q}} + (\mathbf{K} + \mathbf{K}_G) \cdot \mathbf{q} = \mathbf{Q}_v + \mathbf{Q}_g \quad (2.4)$$

\mathbf{K}_G is the geometric stiffness matrix. The section of the \mathbf{K}_G matrix belonging to each blade is calculated symbolically, assuming that each blade is an isolated flexible beam rotating about its endpoint about an axis perpendicular to its plane with rotational speed Ω . For each value of Ω the centrifugal force acting on a blade is assumed to be a constant axial force making \mathbf{K}_G a constant matrix. In this project, axial centrifugal stiffening is neglected to reduce the number of high-frequency modes, which slow down the simulation. The section of the \mathbf{K}_G matrix belonging to the tower is 0 since the tower is not subjected to centrifugal forces.

Flexible bodies

The flexible motion of the tower is described using Rayleigh-Ritz's method, where the deflection \bar{u}_f is described by separating the spatial and time-dependent variables. The time-dependent functions are the flexible generalised coordinates for the given body, and the spatial-dependent functions are shape functions that describe the in-plane modes of the tower. The same shape functions are assumed for the flexible blades, and is shown in Eq. (2.5).

$$\bar{u}_f(\bar{x}, t) = \begin{bmatrix} \phi_{tra}(\bar{x}) & \phi_{rot}(\bar{x}) \end{bmatrix} \begin{bmatrix} \nu(t) \\ \psi(t) \end{bmatrix} = \mathbf{N}(\bar{x}) \mathbf{q}(t) \quad (2.5)$$

Where $\phi_{tra}(\bar{x})$ and $\phi_{rot}(\bar{x})$ are the Hermite cubic polynomials. The kinetic and gravitational potential energies is determined for the tower and blades as shown in Eq. (2.6) and Eq. (2.7), where subscript u denotes the unbalanced masses that has to be taken into account for blade 4 and 5 and \mathbf{r} is a vector that describes the position of the flexed body in relation to the global reference frame.

$$T^1 = \frac{1}{2} \rho_t A_t \int_0^{L_t} \left(\dot{\bar{u}}_f^1(\bar{x}, t) \right)^2 d\bar{x} \quad U_g^1 = g \rho_t A_t \int_0^{L_t} \frac{1}{2} L_t d\bar{x} \quad (2.6)$$

$$T^i = \frac{1}{2} \rho_b A_b \int_0^{L_b} \left(\dot{\mathbf{r}}^i \right)^T \dot{\mathbf{r}}^i d\bar{x} + \frac{1}{2} m_u \left(\dot{\mathbf{r}}_u^i \right)^T \dot{\mathbf{r}}_u^i \quad U_g^i = g \rho_b A_b \int_0^{L_b} r_y^i d\bar{x} + g \cdot m_u^i \cdot r_{y,u}^i \quad (2.7)$$

The elastic potential energy can be determined equally for the tower and blades according to Eq. (2.8).

$$U_{el}^i = \frac{1}{2} E^i I^i \left(\mathbf{q}^i(t) \right)^T \int_0^L \left(\left(\mathbf{N}^{''i}(\bar{x}) \right)^T \mathbf{N}^{''i}(\bar{x}) \right) d\bar{x} \cdot \mathbf{q}^i(t) \quad (2.8)$$

The kinetic and potential energies for the rigid bodies are included in the Lagrange equations, however, they are not presented here because they are trivial.

2.2 Campbell Diagram

Fig. 2.3 shows a Campbell diagram for the RFT-B model for rotational speeds $\Omega=20-450$ rpm. The diagram shows the natural frequencies ω of the tower and the three blades as a function of the rotational speed Ω . In this section, the natural frequencies are obtained by considering each body as an isolated body. Each blade is modelled as a flexible beam rotating about its endpoint with rotational speed Ω , considering the centrifugal force from the rotation. The tower is modelled as a uniform clamped beam with a point mass acting in the free end. This point mass is the sum of the masses of the three blades, the nacelle, the hub and the two unbalanced masses. All bodies are modelled as 1-DOF systems, and therefore they each have one vibrational mode and one corresponding line in the Campbell diagram. For all four flexible bodies, the mode lines are calculated by assuming harmonic oscillation to obtain the response transfer function:

$$\mathbf{H}(\omega, \Omega) = \frac{X}{F} = -[\omega^2 \mathbf{M} + i\omega(\mathbf{C} - \mathbf{D}(\Omega)) + (\mathbf{K} + \mathbf{K}_G(\Omega) - \mathbf{E}(\Omega))]^{-1} \quad (2.9)$$

Solving Eq. (2.9) for all rotational speeds in the range $\Omega=20-450$ rpm and all excitation frequencies in the range $\omega=0-20$ Hz yields the plots in Fig. 2.2. Here the transfer function from Eq. (2.9) is shown for the RFT-B blade 4 (a) and tower (b). For each body in Fig. 2.2 the peaks show the body's natural frequency for various rotational speeds.

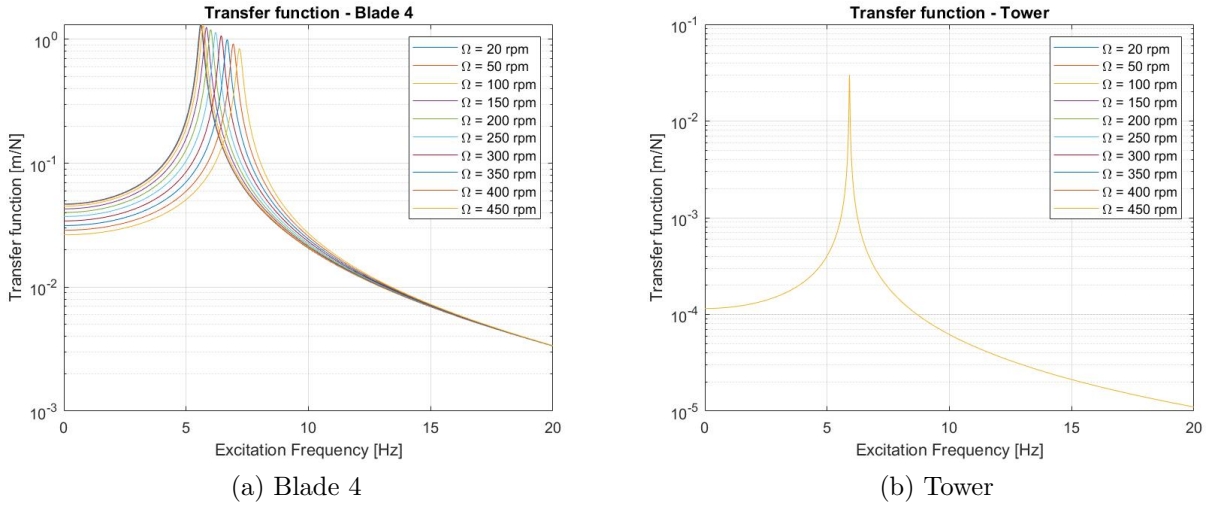


Figure 2.2: Response transfer function for the RFT-B blade 4 and tower

In the Campbell diagram, the rays spreading out from the origin represent integer multipliers (from 1-5) of the rotational speed of the blades. Note that the unit is [rpm] on the X-axis and [Hz] on the Y-axis. At intersection points between a body's mode line and an integer multiplier, the body is excited at the same frequency as its natural frequency ω or a higher harmonic of ω . At these points, it is possible for resonance to occur. When designing a structure, the Campbell diagram is used to avoid these points of resonance. The higher harmonics are represented in the integer multipliers from 2-4.

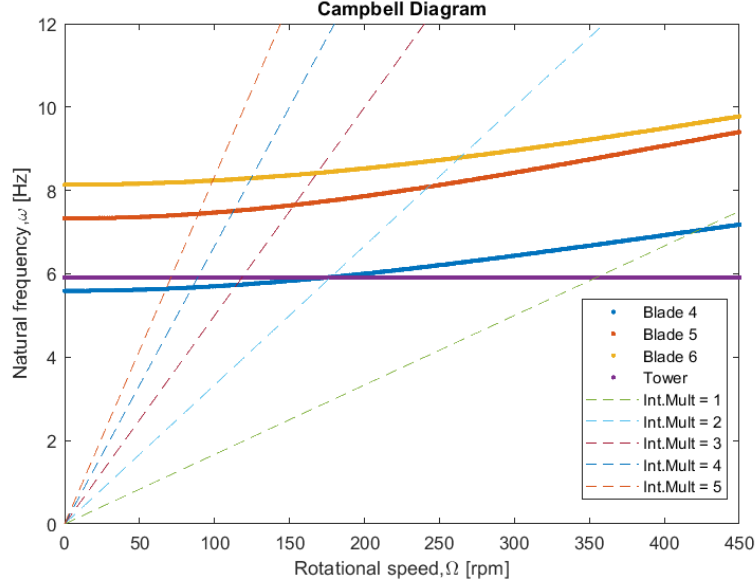


Figure 2.3: Campbell diagram showing natural frequencies as a function of rotational speed for the flexible bodies, along with relevant integer multipliers.

In the Campbell diagram on Fig. 2.3 the natural frequency for each blade takes the shape of a curved line with a positive slope. The centrifugal force from the rotation has a stiffening effect on the blades. When Ω increases, the centrifugal force increases, which also increases the natural frequency of the blade. This is shown in Fig. 2.2 (a). In the Campbell diagram, the natural frequency of blade 4 is significantly lower than for blade 5 and 6. Also, the frequency of blade 5 is lower than for blade 6. This is explained by the unbalanced masses. For blade 4 the mass of the unbalance is $m_{u4} = 12.5$ g and the eccentricity is $d_{m4} = 45$ cm, and for blade 5 these parameters are $m_{u5} = 16.7$ g and $d_{m5} = 22.5$ cm. Considering each blade as a clamped cantilever beam, the static beam deflection is proportional to the mass m_u in the first power and the eccentricity d_m in the second power. Bending stiffness is defined as the ratio between vertical force and vertical deflection; when the deflection increases, the bending stiffness decreases, causing the natural frequency to decrease.

In the Campbell diagram on Fig. 2.3 the tower's natural frequency is a vertical line. Due to the way the tower is modelled in this section, the natural frequency of the tower ω_t is independent of the rotational speed Ω . This is shown in Fig. 2.2 (b). In the tower, considering the intersection lines with the first two integer multipliers, resonance will occur around the rotational speeds $\Omega = 355$ rpm and $\Omega = 177.5$ rpm. In the next sections, the RFT-B is simulated with all bodies in one complex system. Here, the tower's resonance frequencies from the Campbell diagram are compared to the complex model, to examine how the tower is affected by the flexibility of the blades.

2.3 Lateral Dynamic Response of Tower $\Omega = 120$ rpm

The RFT-B model is simulated for firstly, a rotational speed of $\Omega = 120$ rpm for 50 seconds. From the time domain solution, the lateral acceleration \ddot{v}^1 is plotted as shown in Fig. 2.4 (a). It is clear, that the transient response of the acceleration dies out after approximately 15 s, as it reaches steady state. For post-processing, it is only the steady state part of the acceleration that is used.

The obtained acceleration signal consist of main dynamic contributions from the unbalance and the flexibility of the blades. To verify the acceleration signal in terms of the unbalance, it is compared to a 1-DOF model of the same system, where the rotor is treated as a rigid body and the tower is modelled as a beam with equivalent mass m_{eq} and spring constant k_{eq} . The acceleration amplitude of the 1-DOF model is determined using Eq. (2.10) and is also shown on Fig. 2.4 (a). In Eq. (2.10) m_e is the eccentric masses, e is the eccentricity and m_{tot} is the equivalent mass of the tower and the masses of the nacelle, hub and blades.

$$\ddot{X} = -X \cdot \Omega^2 = - \left(\frac{m_e \cdot e \cdot \Omega^2}{-\Omega^2 \cdot m_{tot} + k_{eq}} \right) \cdot \Omega^2 \quad (2.10)$$

As it can be read from the plot, the 1-DOF acceleration amplitude validates the steady state acceleration signal, as the two amplitudes are similar. The small difference is a result of the simplifications made in the 1-DOF model.

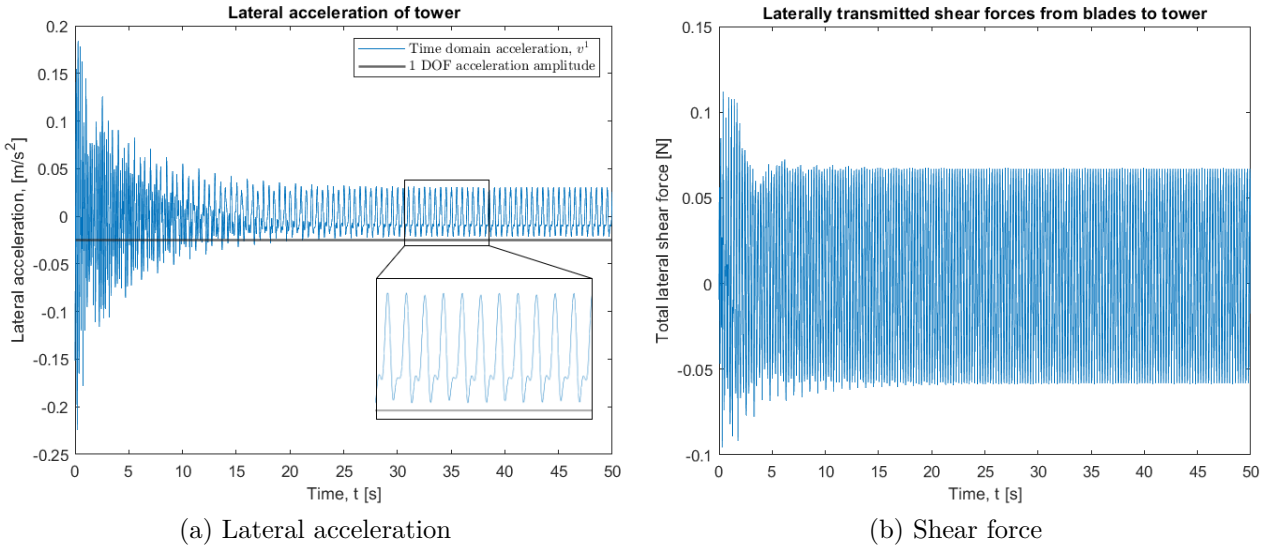
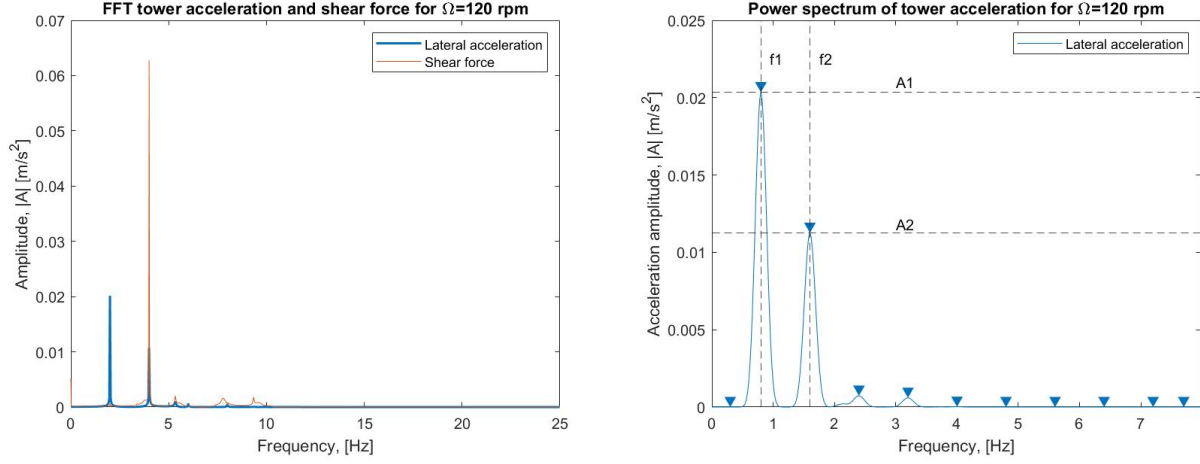


Figure 2.4: Lateral acceleration for RFT-B model and total laterally transmitted shear force from the blades to the tower.

Verification of the acceleration signal in terms of flexibility is done by looking at the total laterally transmitted shear force from the blades to the tower. The shear force of each blade is determined using Eq. (2.11), which acts perpendicular to the blade and is therefore projected to Y^1 , see Fig. 2.1, to get the shear force contribution to the tower. The total lateral shear force of the tower is shown in Fig. 2.4 (b).

$$V = \left(\frac{\partial^3 \mathbf{N}_y}{\partial x^3} \right) \mathbf{q} \quad (2.11)$$

The lateral excitation of the tower from the flexibility of the blades is equal to the shear force of the tower. This can be shown by performing a FFT on both the lateral acceleration and shear force, as shown in Fig. 2.5 (a). From this plot, it can be read that the one main frequency of the shear force is equal to the second main frequency of the lateral acceleration. Since the first main frequency of the lateral acceleration has an amplitude equal to the overall amplitude, which describes the contribution from the unbalance, the second frequency must be the contribution from the flexibility. Fig. 2.5 (b) shows the equivalent power spectrum for the lateral acceleration with a frequency resolution of 0.4 Hz. The amplitude peaks ($A1$, $A2$) and the corresponding frequencies ($f1$, $f2$) are automatically detected.



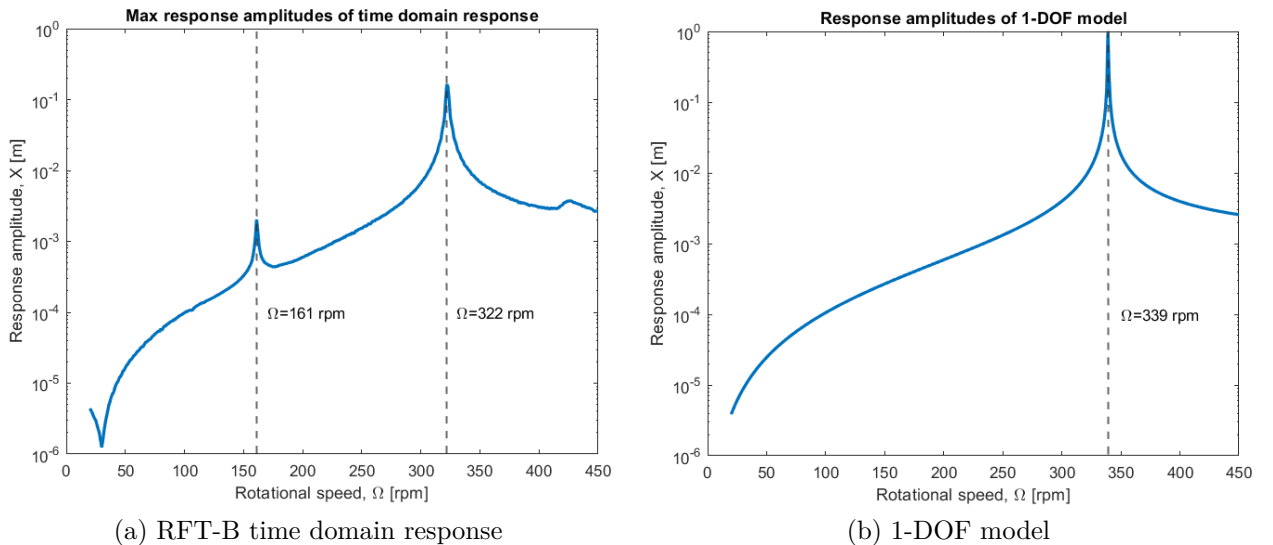
(a) FFT spectrum of lateral acceleration/shear force (b) Power spectrum of lateral acceleration with peaks

Figure 2.5: FFT and power spectrum on lateral acceleration and shear force.

Fig. 2.4 (a) shows that the laterally transmitted shear from the blades to the tower causes a deterministic periodic acceleration that is not harmonic. By performing a FFT on the lateral acceleration the function is considered as a linear series of harmonics; the main harmonic has the same frequency as the fundamental frequency, and the higher harmonics have frequencies that are multipliers of the fundamental frequency. The FFT spectrum in Fig. 2.5 shows that the response is dominated only by the main harmonic and the first higher harmonic. It is normal that the higher harmonics have low amplitudes and contribute little to the response waveform.

2.4 Lateral Dynamic Response of Tower $\Omega = 20 - 450$ rpm

The RFT-B model is now simulated for a range of rotational speeds $\Omega = 120 - 450$ rpm for 50 seconds. From the time domain solution the maximum steady state response amplitudes for each Ω is plotted, as shown in Fig. 2.6 (a), in order to investigate the critical rotational speeds of the system. From the figure, it can be read that resonance occurs at two main critical speeds of $\Omega = 161$ rpm and $\Omega = 322$. The amplitude is also affected at a rotational speed of $\Omega = 424$.



(a) RFT-B time domain response

(b) 1-DOF model

Figure 2.6: Response amplitudes as a function of rotational speed.

For comparison, the response amplitudes of the 1-DOF model is also shown in Fig. 2.6 (b). The response amplitude X is determined using Eq. (2.10) for each rotational speed. The analytical solution assumes that the system only has one natural frequency, since it is modelled as one mass, for which reason there only is one peak. The peak occurs at $\Omega = 339$ rpm, which is slightly different from one obtained with the RFT-B model, but this difference is a result of the simplifications in the 1-DOF model and resolution of the simulation.

As explained in Section 2.3, the lateral acceleration is governed by two dominating dynamic features: (1) the excitation from the unbalanced masses and (2) the excitation from the lateral shear force caused by the flexibility of the blades. The two peaks shown in Fig. 2.6 (a) correspond to the two dominating dynamic features in the model. The response of each dynamic feature is clearly dependent on the rotational speed Ω . In the time domain lateral acceleration, it is possible to isolate the maximum acceleration amplitude belonging to the dominating features. Doing this, the origin of each peak in Fig. 2.6 (a) can be explained. For each rotational speed $\Omega = 20 - 450$ rpm, the lateral acceleration is analyzed using a power spectrum with a frequency resolution of 0.4 Hz. For all values of Ω the power spectrum features two dominating peaks. The left peak corresponds to the first dynamic feature from the unbalanced masses, and the right peak corresponds to the second dynamic feature from the flexible blades.

As shown in Fig. 2.5 (b) the amplitude peaks belonging to each feature ($A1$, $A2$) and the corresponding frequencies ($f1$, $f2$) can be automatically detected and stored. Doing this for all rotational speeds yields the two plots shown in Fig. 2.7. Plot (a) shows the frequency of the dominating features f in Hz vs. Ω in rpm and plot (b) shows the acceleration amplitude of the dominating features A in m/s^2 vs. Ω in rpm.

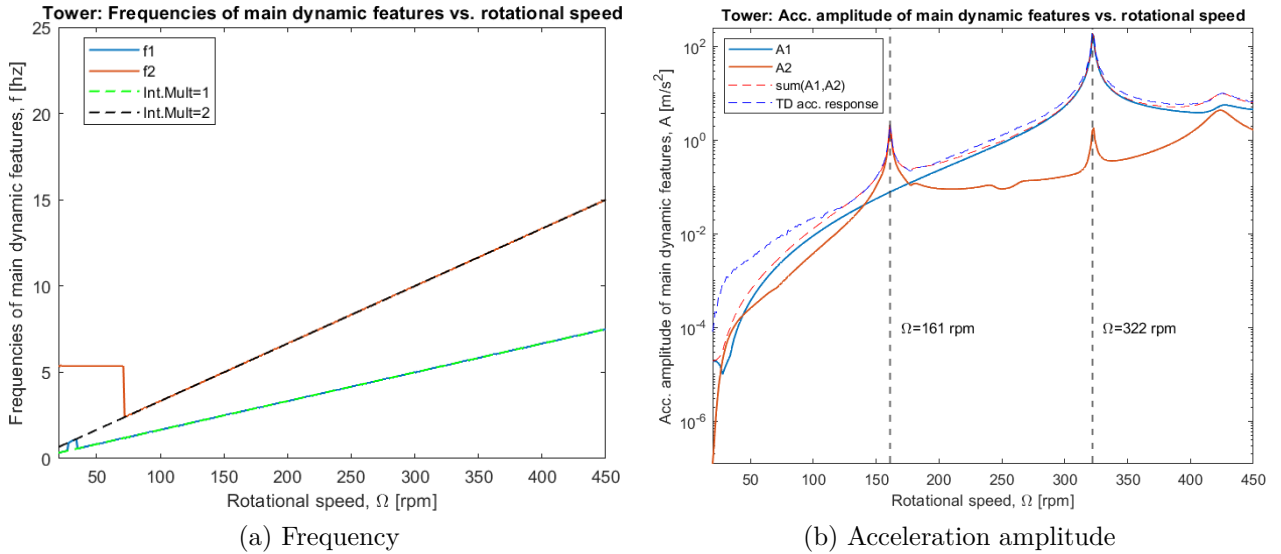


Figure 2.7: Frequency and acceleration amplitudes as a function of rotational speeds for the main dynamic features of RFT-B

In Fig. 2.7 (a) the frequencies are uneven for low rotational speeds, but for speeds $\Omega \geq 70$ rpm both dominating frequencies assume the shapes of straight lines fanning out from the origin. As expected these lines are coincident with the first two integer multipliers in the Campbell diagram in Fig. 2.3. When the rotational speed assumes either the value of the towers fundamental frequency or its first higher harmonic, resonance occurs and the acceleration amplitude spikes.

In Fig. 2.7 (b) the acceleration amplitude spikes at the same speeds $\Omega = 161$ rpm and $\Omega = 322$ rpm as in Fig. 2.6, where the amplitudes are obtained without isolating the dynamic features.

By examining Fig. 2.7 (b) it is clear that the first peak at $\Omega = 161$ rpm originates from the shear force caused by the flexibility of the blades, and the second peak at $\Omega = 322$ rpm originates from the unbalanced masses on the blades. In the figure, the dotted orange line represents the resulting sum of the amplitudes for every Ω . The dotted blue line represents acceleration amplitudes obtained without isolating the dynamic features. Preferably, these dotted lines should coincide. As for Fig. 2.7 (a), the results are very good for speeds $\Omega \geq 70$ rpm.

2.5 Fatigue damage of the blades

A fatigue analysis is performed on the blades in order to determine the critical rotational speed for $\Omega = 20 - 450$ rpm in terms of the blades lifetime. The SN-curve used is on the form: $N = K \cdot \sigma^m$, where the parameters are assumed to be $K = 10^{15.3}$ and $m = -5$. The maximum bending stress, σ , is determined from the maximum shear force at each rotational speed, which is determined using Eq. (2.11). The shear force acts at the end of the blades and creates a moment at the root, from which the bending stress is determined as follows.

$$\sigma_i = \frac{V_i^{max} \cdot L_b \cdot h_b}{2 \cdot I_b} \quad (2.12)$$

In the above equation I_b is the area moment of inertia and h_b is the height of the blade. Since the Fig. 2.8 shows the maximum bending stresses of the three blades and the corresponding number of cycles. For each blade, the bending stress resulting in the lowest lifetime is highlighted and the corresponding rotational speed that relates to the maximum bending stress and shear force is shown.

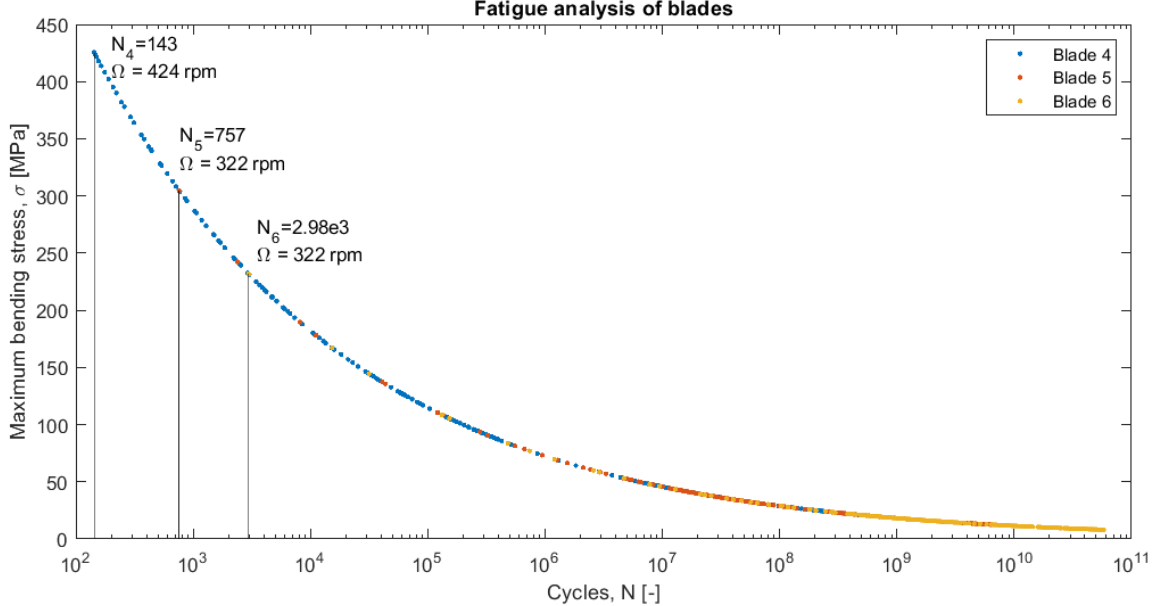


Figure 2.8: Bending stress amplitudes as a function of number of cycles of blades 4, 5 and 6

From Fig. 2.8 it can be read that blade 4 has the lowest lifetime of 143 cycles at rotational speed $\Omega = 424$ rpm, whereas blades 5 and 6 are expected to have the lowest lifetime at rotational speed $\Omega = 322$ rpm. It is reasonable that blade 4 is expected to have the lowest lifetime, since this blade has an unbalance with greater eccentricity. The critical rotational speeds are consistent with Fig. 2.6 (a) and Fig. 2.7 (b), since resonance occurs at $\Omega = 322$ rpm and an significant increase in amplitude also can be seen at $\Omega = 424$ rpm.

2.6 Conclusion

In the second part of the project, a 2D model of a rotor with flexible tower and unbalanced flexible blades is simulated using flexible coordinates. The lateral dynamic response of the tower is dominated by two dynamic features, one from the unbalanced masses and one from the lateral shear force caused by the flexibility of the blades. These two features peak at rotational speeds $\Omega=161$ rpm and $\Omega=322$ rpm. This corresponds to the tower's natural frequency and a higher harmonic. A lifetime assessment of the blades, show that blade 4 has the shortest lifetime of 143 cycles at $\Omega=424$ rpm. The other blades have their shortest lifetime for $\Omega=322$ rpm.